**Tenth International Conference on Computational Fluid Dynamics (ICCFD10), Barcelona, Spain, July 9-13, 2018** **ICCFD10-054**

# Development of linear unstable modes in supersonic streamwise vortices using a weighted essentially non-oscillatory scheme

T. Hiejima*
Corresponding author: hiejima@aero.osakafu-u.ac.jp

* Aerospace Engineering, Osaka Prefecture University, Sakai, Osaka 599-8531, JAPAN

**Abstract:** Growth processes in supersonic streamwise vortices with linear unstable modes at Mach number 2.5 were numerically investigated using a weighted compact nonlinear scheme (WCNS) with three different accuracies. In the evolution of the inviscid linear unstable mode $m = -6$, the growth rate and eigenfunction profiles of the mode numerically resolved were generally consistent with those obtained with the linear stability theory (LST) during the early transition stage, regardless of the computational accuracy. However, the numerical results shown obtained by nonlinear developments differed according to the accuracy. Among the different accuracies under the same grid resolution, the ninth-order accuracy scheme for the interpolation of primitive variables was able to capture small vortical structures at the downstream in the supersonic flow. In addition, the negative circulation generated and the total disturbance energy indicated that such high accuracy is effective in resolving the developed flow in supersonic vortices, even at moderate grid resolutions.

*Keywords:* Supersonic Flow, Batchelor Vortex, Linear Stability Analysis, Direct Numerical Simulation.

## 1 Introduction

The main issue in the field of supersonic combustion ramjet (scramjet) engine is to achieve effective fuel-oxidizer mixing in the engine over the short time scale of combustion [1]. Mixing in supersonic flows is effectively enhanced by using axial vorticities such as streamwise vortices. One of the reasons is that the vortices may relax a compressibility effect [2–6], which reduces fluctuation growth. Although streamwise vortices are core structures in turbulent transitions, the transition mechanism remains unclear except for low-speed flows. Thus, understanding it is important to enhance the mixing ability and to enable a turbulence control in high-speed flows. Figure 1 shows a relation between the growth property of streamwise vortices and the compressibility obtained from the results of a previous work [7] about the development of random disturbances. Using a rate derived from the amplitude of the axial vorticity disturbance as $\beta_M = \ln(|\Omega_x|/|\Omega_x|_{X=0})$, the longitudinal axis is $\beta_M/\beta_{M0}$, normalized by the rate corresponding to an incompressible case, and the abscissa axis is the absolute value of entropy gradient $|ds/dr|$ in a streamwise vortex. The result indicates that as the Mach number increases, $|dS/dr|$ increases, and the rate decreases without so much as decreasing rates in mixing layer. It is noteworthy that the rate decreases a little in isentropic cases. Thus, this figure provides an intriguing result for compressibility and entropy effects. So far, the study of thermodynamics of supersonic streamwise vortices has been superficial. To deepen the understanding of compressibility effects, it is also essential to study the fundamental development of unstable modes in supersonic streamwise vortices.

A high-accuracy simulation is needed to capture developing three-dimensional disturbance structures, i.e., a number of spiral vortex structures, and those interactions appearing in the evolution of such streamwise vortices. Both weighted essentially non-oscillatory (WENO) and weighted compact nonlinear schemes

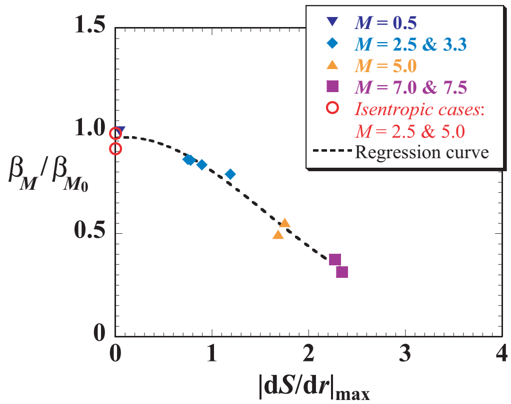


Figure 1: Relation between the growth property of streamwise vortices and the compressibility, obtained from the results of a previous work [7].

(WCNS) are high-resolution finite-difference schemes used for supersonic flows with shock waves. The WENO scheme is excellent in accurately capturing a shock wave [8, 9], and the WCNS also has flexibility in choosing a numerical flux, which is separated into several classes when computing compressible flows. Deng and Zhang [10] were the first to develop the WCNS, which was then extended as a high-order version [11–13]. The interactions between supersonic streamwise vortices and oblique shock waves are solved with good accuracy using the scheme published in [14] for difficult instances.

In streamwise vortex transitions, although the development of unstable modes was studied using an incompressible Batchelor vortex [15–17], the downstream states of spatially developing vortices has not been clarified either. In this study, the spatial development of supersonic streamwise vortices with a liner unstable mode was investigated in terms of computational accuracy and grid resolution by using the WCNS. For the azimuthal wavenumber $m = -4$, the numerically resolved growth rate and eigenfunction profiles were in good agreement with those obtained from the linear stability theory (LST) [18]. However, the evolution of a higher-wavenumber mode, which would need a higher resolution, has not been investigated. In addition, it is unknown whether downstream structures obtained from such evolution are numerically valid.

This paper is organized as follows. Section II describes the basic flow of the supersonic streamwise vortices. The LST for the vortices is explained in Section III. Section IV describes the numerical method based on a WCNS scheme including the high-order differential accuracies and computational conditions. Section V presents the results and provides a discussion on the vortices developed by varying the accuracies and the grid resolution at Mach number 2.5. The conclusions are presented in Section VI.

## 2 Supersonic Batchelor vortex

The Batchelor vortices [19] are used to investigate the fundamental transition of supersonic streamwise vortices because their profiles are compatible with many swirling flows at high Reynolds numbers (see, for instance, [20]). In the cylindrical polar coordinates, the radial, azimuthal, and axial velocities ($u_r$, $u_\theta$ and $u_x$, respectively) of the Batchelor vortex were given as follows:

$$u_r(r) = 0, \quad u_\theta(r) = M_\infty \frac{q}{r}\left[1 - \exp(-r^2)\right], \quad u_x(r) = M_\infty[1 - \mu \exp(-r^2)], \tag{1}$$

where $q$ and $\mu$ denote the swirl intensity (circulation) and axial velocity deficit, respectively, and $M_\infty$ is the freestream Mach number. These velocities were normalized with the freestream speed of sound $c^*_\infty$. The density $\rho(r)$ and pressure $p(r)$ required for supersonic conditions in basic inviscid steady flows were calculated as follows:

$$\frac{dp}{dr} = \rho \frac{{u_\theta}^2}{r}, \quad \frac{d\rho}{dr} = \frac{\rho}{\gamma}\left(\frac{1}{p}\frac{dp}{dr} - \frac{ds}{dr}\right), \tag{2}$$

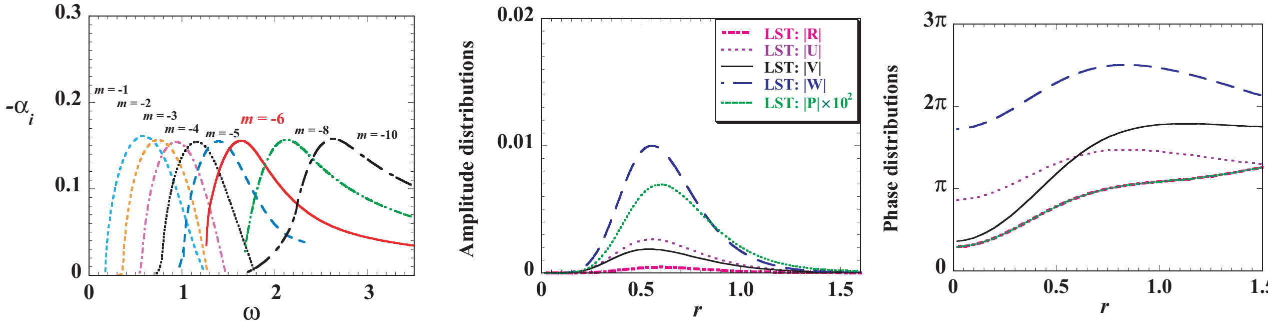


(a) (b)

Figure 2: Results of LST at $M_\infty = 2.5$, $q = 0.16$, and $\mu = 0.5$. (a) Relations between the growth rate and the angular frequency, $-\alpha_i$ vs. $\omega$, and (b) amplitude and phase profiles of the disturbance, density $R$, velocities $U, V, W$, and pressure $P$ for $m = -6$.

where $s$ is the entropy and $\gamma$ is the ratio of the specific heats. The entropy gradient in Eq. (2) was obtained under isentropic condition.

# 3 Linear stability analysis

This section describes an inviscid linear stability of streamwise vortices in Section 2. Based on the normal modes, the linear disturbances were as follows:

$$\{\widetilde{\rho}, \widetilde{u}_r, \widetilde{u}_\theta, \widetilde{u}_x, \widetilde{p}\} = \{R(r), U(r), V(r), W(r), P(r)\}\exp[\boldsymbol{i}(\alpha x + m\theta - \omega t)], \tag{3}$$

where $m$ is the azimuthal wavenumber (integer), $\omega$ is the angular frequency, $\alpha_r$ is the axial wavenumber, $-\alpha_i$ is the spatial growth rate, and $\alpha = \alpha_r + \boldsymbol{i}\,\alpha_i$ (complex). The inviscid linearized disturbance equations were written as follows [21]:

$$\frac{dP}{dr} = A(r)P + B(r)U, \ \frac{dU}{dr} = C(r)P + D(r)U, \tag{4}$$

$$\begin{aligned} A(r) &= \frac{{u_\theta}^2}{r\,c^2} - \frac{2mu_\theta}{r^2\sigma}\,,\ B(r) = \frac{\boldsymbol{i}\,\rho}{\sigma}\left(N^2 + \frac{2u_\theta\omega_x}{r} - \sigma^2\right), \\ C(r) &= \frac{\boldsymbol{i}}{\rho\,\sigma}\left(\alpha^2 + \frac{m^2}{r^2} - \frac{\sigma^2}{c^2}\right),\ D(r) = \frac{1}{\sigma}\left(\frac{m}{r}\omega_x - \alpha\,\omega_\theta\right) - \frac{{u_\theta}^2}{r\,c^2} - \frac{1}{r}, \end{aligned} \tag{5}$$

$$\sigma = -\omega + m\frac{u_\theta}{r} + \alpha u_x,\ \omega_x = \frac{du_\theta}{dr} + \frac{u_\theta}{r},\ \omega_\theta = -\frac{du_x}{dr},\ N^2 = -\frac{{u_\theta}^2}{\gamma\,r}\frac{ds}{dr}, \tag{6}$$

where $\sigma$ is the Doppler frequency, $\omega_x$ is the axial vorticity, $\omega_\theta$ is the azimuthal vorticity, $N$ is the Brunt–Väisälä frequency, and $c = \sqrt{\gamma p/\rho}$ is the local speed of sound. Equation (4) and the boundary conditions at both origin ($r = 0$) and infinity ($r \to \infty$) form an eigenvalue problem for the complex $\alpha$.

The instability characteristics of the Bachelor vortex were obtained from this LST. Figure 2(a) shows $-\alpha_i$ as a function of $\omega$ for $q = 0.16$ and $\mu = 0.5$ at $M_\infty = 2.5$. The effect of $m$ on the maximum growth rate was small and the profiles only differed in band frequency. As a high wavenumber, Fig. 2(b) plots the eigenfunctions (amplitude and phase) of the perturbations for $m = -6$. The dominant disturbance was the axial velocity perturbation and the phase profiles changed near the inflectional point of the axial velocity. The density disturbance was identical to the pressure disturbance in phase because of its isentropic property.

# 4 Numerical methods

## 4.1 Governing equations

To analyze both linear and nonlinear developments of supersonic streamwise vortices via a full simulation, the viscous term was also considered. The governing equations were the three-dimensional, unsteady and compressible Navier–Stokes equations in general coordinates $\xi_i$ ($i$ = 1–3) as follows:

$$\frac{\partial}{\partial t}\left(\frac{\boldsymbol{Q}}{J}\right) + \frac{\partial \boldsymbol{F}_i}{\partial \xi_i} = \frac{\partial \boldsymbol{F}_{v\,i}}{\partial \xi_i}, \tag{7}$$

$$\boldsymbol{Q} = \begin{bmatrix} \rho \\ \rho\,u_1 \\ \rho\,u_2 \\ \rho\,u_3 \\ e \end{bmatrix}, \; \boldsymbol{F}_i = \begin{bmatrix} \rho\,U_i \\ \rho\,u_1\,U_i + p\,(J^{-1}\partial\xi_i/\partial x_1) \\ \rho\,u_2\,U_i + p\,(J^{-1}\partial\xi_i/\partial x_2) \\ \rho\,u_3\,U_i + p\,(J^{-1}\partial\xi_i/\partial x_3) \\ (e+p)\,U_i \end{bmatrix}, \; U_i = \left(J^{-1}\frac{\partial \xi_i}{\partial x_k}\right) u_k, \tag{8}$$

$$\boldsymbol{F}_{v\,i} = \begin{bmatrix} 0 \\ \tau_{11}\,(J^{-1}\partial\xi_i/\partial x_1) + \tau_{12}\,(J^{-1}\partial\xi_i/\partial x_2) + \tau_{13}\,(J^{-1}\partial\xi_i/\partial x_3) \\ \tau_{21}\,(J^{-1}\partial\xi_i/\partial x_1) + \tau_{22}\,(J^{-1}\partial\xi_i/\partial x_2) + \tau_{23}\,(J^{-1}\partial\xi_i/\partial x_3) \\ \tau_{31}\,(J^{-1}\partial\xi_i/\partial x_1) + \tau_{32}\,(J^{-1}\partial\xi_i/\partial x_2) + \tau_{33}\,(J^{-1}\partial\xi_i/\partial x_3) \\ \beta_1\,(J^{-1}\partial\xi_i/\partial x_1) + \beta_2\,(J^{-1}\partial\xi_i/\partial x_2) + \beta_3\,(J^{-1}\partial\xi_i/\partial x_3) \end{bmatrix},$$

$$\begin{aligned} J^{-1} = {} & \frac{\partial x_1}{\partial \xi_1}\left(\frac{\partial x_2}{\partial \xi_2}\frac{\partial x_3}{\partial \xi_3} - \frac{\partial x_2}{\partial \xi_3}\frac{\partial x_3}{\partial \xi_2}\right) + \frac{\partial x_1}{\partial \xi_2}\left(\frac{\partial x_2}{\partial \xi_3}\frac{\partial x_3}{\partial \xi_1} - \frac{\partial x_2}{\partial \xi_1}\frac{\partial x_3}{\partial \xi_3}\right) \\ & + \frac{\partial x_1}{\partial \xi_3}\left(\frac{\partial x_2}{\partial \xi_1}\frac{\partial x_3}{\partial \xi_2} - \frac{\partial x_2}{\partial \xi_2}\frac{\partial x_3}{\partial \xi_1}\right), \end{aligned}$$

where $\boldsymbol{Q}$ is the vector of conservative variables, $\boldsymbol{F}_i$ and $\boldsymbol{F}_{v\,i}$ indicate convective and viscous fluxes, respectively. $U_i$ represent the velocity components at the cell interface, $J$ is the Jacobian that transforms the coordinates from the physical space into the computational space, $J^{-1}$ corresponds to the cell volume in the physical space, provided that all cell volumes in computational space are equal to unity, and $J^{-1}\partial\xi_i/\partial x_k$ to the derivatives for the coordinate conversion, namely, the metrics:

$$\begin{aligned} p &= \rho\,T, \quad e = \frac{p}{\gamma-1} + \frac{1}{2}\rho\,u_k\,u_k\,, \\ \tau_{ij} &= \frac{\eta(T)}{Re_M}\left(\frac{\partial u_i}{\partial x_j} + \frac{\partial u_j}{\partial x_i} - \frac{2}{3}\delta_{ij}\frac{\partial u_k}{\partial x_k}\right), \\ \dot{q}_i &= -\frac{\gamma}{(\gamma-1)}\frac{\eta(T)}{Re_M\,Pr}\frac{\partial T}{\partial x_i}, \quad \beta_i = u_i\,\tau_{ij} + \dot{q}_i, \end{aligned} \tag{9}$$

Here, $e$ is the total energy, $\tau_{ij}$ is the viscous stress tensor, $\dot{q}_i$ is the conductive heat flux, and $u_i$ is the velocity component in Cartesian coordinates. The Reynolds number based on the sonic velocity was defined by $Re_M$ $= (\rho^*_\infty\, c^*_\infty\, a^*)/\eta^*_\infty (= Re\,/M_\infty) = 9000$ (the dimensional quantities have the superscript $*$), and the Prandtl number $Pr$ was 0.72. The viscosity $\eta$ was calculated from Sutherland's law,

$$\eta(T) = T^{\frac{3}{2}}\frac{1+\vartheta}{T+\vartheta}, \tag{10}$$

where $\vartheta = 110.4/(\gamma\,T^*_\infty)$ was normalized by the freestream temperature.

## 4.2 Numerical evaluation of convective fluxes

The convective flux terms were discretized using the numerical flux $\boldsymbol{F}_{i,\,s+\frac{1}{2}}$, the cell spacing $\Delta\xi_i$, and the vector of primitive variables $\boldsymbol{q}(=q_j)$ as follows:

$$\frac{\partial \boldsymbol{F}_i}{\partial \xi_i} \equiv \frac{\boldsymbol{F}_{i,\,s+\frac{1}{2}}(\boldsymbol{q}) - \boldsymbol{F}_{i,\,s-\frac{1}{2}}(\boldsymbol{q})}{\Delta\xi_i}\,,\ \boldsymbol{q} = \begin{bmatrix} \rho \\ u_1 \\ u_2 \\ u_3 \\ p \end{bmatrix}. \tag{11}$$

A modified numerical flux $\overline{\boldsymbol{F}}_{i,\,s+\frac{1}{2}}$ was obtained as follows, by multiplying $\boldsymbol{F}_{i,\,s+\frac{1}{2}}$ in Eq. (11) for a transformation matrix $\boldsymbol{T}$,

$$\overline{\boldsymbol{F}}_{i,\,s+\frac{1}{2}} = \frac{1}{\sqrt{(m_i)_k\cdot(m_i)_k}}\boldsymbol{T}\boldsymbol{F}_{i,\,s+\frac{1}{2}} = \begin{bmatrix} \rho\,\hat{U}_i \\ \rho\,\hat{U}\hat{U}_i + p\,\delta_{1i} \\ \rho\,\hat{V}\hat{U}_i + p\,\delta_{2i} \\ \rho\,\hat{W}\hat{U}_i + p\,\delta_{3i} \\ \rho\,H\hat{U}_i \end{bmatrix}_{i,\,s+\frac{1}{2}}, \tag{12}$$

$$\hat{U} = u_k\,(\hat{m}_1)_k,\ \hat{V} = u_k\,(\hat{m}_2)_k,\ \hat{W} = u_k\,(\hat{m}_3)_k,\ H = \frac{e+p}{\rho},$$

$$\boldsymbol{T} = \begin{bmatrix} 1 & 0 & 0 & 0 & 0 \\ 0 & (\hat{m}_1)_1 & (\hat{m}_1)_2 & (\hat{m}_1)_3 & 0 \\ 0 & (\hat{m}_2)_1 & (\hat{m}_2)_2 & (\hat{m}_2)_3 & 0 \\ 0 & (\hat{m}_3)_1 & (\hat{m}_3)_2 & (\hat{m}_3)_3 & 0 \\ 0 & 0 & 0 & 0 & 1 \end{bmatrix},\quad \boldsymbol{T}^{-1} = \begin{bmatrix} 1 & 0 & 0 & 0 & 0 \\ 0 & (\hat{m}_1)_1 & (\hat{m}_2)_1 & (\hat{m}_3)_1 & 0 \\ 0 & (\hat{m}_1)_2 & (\hat{m}_2)_2 & (\hat{m}_3)_2 & 0 \\ 0 & (\hat{m}_1)_3 & (\hat{m}_2)_3 & (\hat{m}_3)_3 & 0 \\ 0 & 0 & 0 & 0 & 1 \end{bmatrix},$$

and then

$$(m_i)_j = J^{-1}\frac{\partial \xi_i}{\partial x_j}\,,\ (\hat{m}_i)_j = \frac{(m_i)_j}{\sqrt{(m_i)_k\cdot(m_i)_k}}\,,\ \hat{U}_i = \frac{1}{\sqrt{(m_i)_k\cdot(m_i)_k}}\,U_i,$$

where $(m_i)_j$ is a vector of metrics and $(\hat{m}_i)_j$ is its unit vector. The unit vectors $(\hat{m}_2)_j$ and $(\hat{m}_3)_j$ represent the vectors perpendicular to $(\hat{m}_1)_j$.

The modified numerical flux in Eq. (12) was evaluated using the AUSMDV scheme [22], which is classified into the Advection Upwind Splitting Method (AUSM) approach and is simple as well as highly accurate. Therefore, the numerical flux was evaluated by substituting Eq. (13) into Eq. (11),

$$\boldsymbol{F}_{i,\,s+\frac{1}{2}} = \sqrt{(m_i)_k\cdot(m_i)_k}\ \boldsymbol{T}^{-1}\overline{\boldsymbol{F}}_{i,\,s+\frac{1}{2}}. \tag{13}$$

In the scheme, the vectors of primitive variables $\boldsymbol{q}_{L,s+\frac{1}{2}}$ and $\boldsymbol{q}_{R,s+\frac{1}{2}}$ are needed; the subscript '$L$' and '$R$' denote the left and right at the cell interface $s+\frac{1}{2}$, respectively.

## 4.3 Nonlinear interpolation with a high-order accuracy

Since this study intends to simulate the development of disturbances in streamwise vortices with acceptable accuracy, the primitive variables $q_j$ need to maintain a high-order spatial accuracy. Therefore, the nonlinear interpolation at the cell interfaces extended by Nonomura and Fujii [12] and the WENO-Z [23] were combined into a high-order accuracy method. The interpolated values were high-order accurate in smooth regions and could also capture large gradients, such as shock waves, without degrading the precision of space differences. Using the Taylor series expansion of the primitive variable $q_j = q(\xi)$, the general interpolation in the cell $[i-1/2, i+1/2]$ was written as:

$$q(\xi) = q_i + (\xi-\xi_i)\left.\frac{\partial q}{\partial \xi}\right|_i + \frac{1}{2}(\xi-\xi_i)^2\left.\frac{\partial^2 q}{\partial \xi^2}\right|_i + \cdots, \tag{14}$$

The stencils of $(2r-1)$ points were needed in the $(2r-1)$th-order interpolation and composed of $r$-points substencils. For each substencil $k(=1,2,\cdots,r)$, the $r$th-order interpolated values of $q^k_{i+\frac{1}{2}}$ were given by

$$q^k_{L,i+\frac{1}{2}} = \quad q_i + \sum_{n=1}^{r-1} \frac{1}{n!}\left(\frac{\Delta\xi}{2}\right)^n \left.\frac{\partial^n q^k}{\partial \xi^n}\right|_i + O((\Delta\xi)^r), \qquad (n=1,2,\cdots,r-1), \tag{15}$$

$$q^k_{R,i+\frac{1}{2}} = q_{i+1} + \sum_{n=1}^{r-1} \frac{1}{n!}\left(\frac{-\Delta\xi}{2}\right)^n \left.\frac{\partial^n q^k}{\partial \xi^n}\right|_{i+1} + O((\Delta\xi)^r), \qquad (n=1,2,\cdots,r-1), \tag{16}$$

where the $n$-th derivatives of $q^k$ are rewritten as the differential operator $L^n(q^k_i)$ as follows:

$$L^n(q^k_i) \equiv \left.\frac{\partial^n q^k}{\partial \xi^n}\right|_i = \left(\frac{1}{\Delta x}\right)^n \sum_{l=1}^{r} c_{n,k,l}\, q_{i+k-r+l-1}. \tag{17}$$

For details on the coefficient $c_{n,k,l}$, see Ref. [12]. To find $(2r-1)$th-order accurate interpolations, Eqs. (15) and (16) were multiplied by the weight coefficient $\omega^k$, and then linearly-coupled, giving

$$\begin{aligned} \hat{q}_{L,i+\frac{1}{2}} &= \sum_{k=1}^{r} \omega^k_L\, q^k_{L,i+\frac{1}{2}}, \\ \hat{q}_{R,i+\frac{1}{2}} &= \sum_{k=1}^{r} \omega^k_R\, q^k_{R,i+\frac{1}{2}}. \end{aligned} \tag{18}$$

The weight coefficients $\omega^k_L$ and $\omega^k_R$ were defined by

$$\omega^k_L = \frac{\alpha^m_L}{\sum_{m=1}^{r} \alpha^m_L}, \quad \omega^k_R = \frac{\alpha^m_R}{\sum_{m=1}^{r} \alpha^m_R}, \tag{19}$$

where they were estimated by the WENO-Z nonlinear weights [23, 24] as follows:

$$\alpha^k_L = C^k_L \left[1 + \frac{\tau_{2r-1}}{IS_k + \varepsilon}\right], \tag{20}$$

$$\tau_{2r-1} = \begin{cases} |IS_1 - IS_r|, & \mathrm{mod}(r,2) = 1 \\ |IS_1 - IS_2 - IS_{r-1} + IS_r|, & \mathrm{mod}(r,2) = 0 \end{cases}. \tag{21}$$

Hence, $C^k_L$ and $C^k_R$ depend on the accuracy [12]. As a smooth indicator adjusting the weight coefficients, the following equation is used here:

$$IS_k = \sum_{l=1}^{r-1} \left[(\Delta x)^l L^l(q^k_i)\right]^2. \tag{22}$$

If there is a discontinuity of variable, the value of $IS_k$ increases depending on the degree of the discontinuity at the position. As a result, the numerical oscillation is avoided because the weight coefficients are close to zero. A small number $\varepsilon = 10^{-10}$ was added to the denominator of Eq. (21) to avoid the zero denominator. Thus, the vectors of primitive variables at the cell interfaces were determined from Eq. (18).

## 4.4 Computing conditions

As mentioned above, the convective flux was evaluated using the AUSMDV and the WCNS schemes with an $mth$-order accuracy for the interpolation of primitive variables at cell interfaces. The viscous flux terms were calculated with an $nth$-order accuracy by a central-difference method. Three accuracy cases (5th-4th, 7th-6th, and 9th-8th) were considered; the different accuracies were denoted by $mth$-$nth$. The temporal

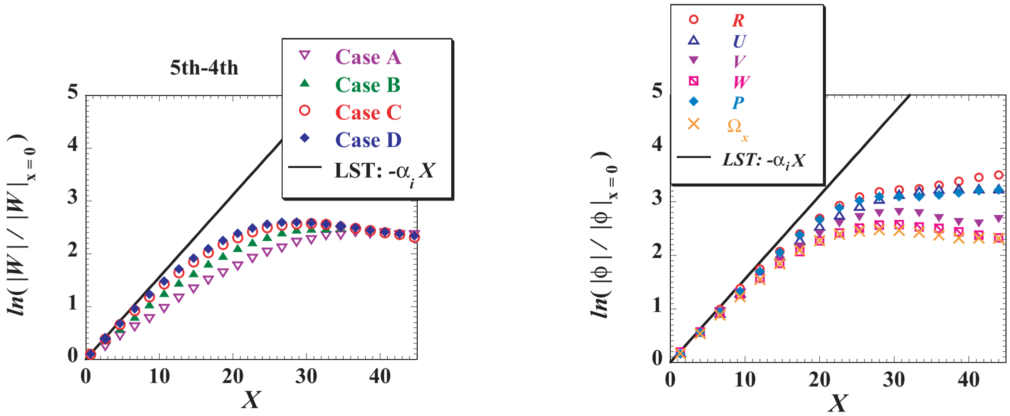


Figure 3: Streamwise variations in the growth rate using 5th-4th for the unstable mode $m = -6$ at $M_\infty = 2.5$, $q = 0.16$, and $\mu = 0.5$; (left) axial velocity disturbance $W$ in various grids and (right) disturbances in density, radial velocity, azimuthal velocity, axial velocity, and axial vorticity, respectively, in case C.

integration adopted a four-step, fourth-order accuracy scheme [25].

The flow was introduced in the $x$-direction, and the physical domain was a rectangular box with sides $L_x = 200$ and $L_y = L_z = 40$. The computational space was also a rectangular box composed of grids of uniform width equal to unity ($\Delta\xi_i = 1$). The grid spacing was uniform in a space that is three times the diameter of the vortex core (the vortex core radius is close to the site of the maximum azimuthal velocity) and centered on the vortex axis; beyond this region, the grid splayed out at irregular intervals. The spatial resolution ($N_x \times N_y \times N_z$) is shown in Table 1.

The supersonic inflows were fixed Batchelor vortices for the swirl intensity $q = 0.16$ and the axial velocity deficit $\mu = 0.5$ with the addition of the linear disturbance of $m = -6$ at Mach number $M_\infty = 2.5$. The maximum amplitude of the disturbance was set to 1 % of the mainstream flow amplitude. The disturbance wavenumber was chosen to inquire into the computational accuracy with a high wavenumber. This $M_\infty$ corresponds to a Mach number coming into the combustor of a supersonic ramjet engine, which represents about one third of flight Mach number [1]. Moreover, based on the circulation value of a streamwise vortex formed by a strut device [26], the maximum circulation was about $q \approx 0.2$. The outflow condition at the outlet, where the flows are supersonic, was extrapolated to the zeroth order. To carry out the simulation for isolated vortices without a contaminated center, symmetry conditions were applied at the boundary surfaces at the $y$–$z$ cross section.

## 5 Results and Discussion

Figure 3 shows the streamwise variations in the growth rate obtained by integrating the disturbance amplitude profile obtained from the flow field using a Fourier decomposition of the $m = -6$ mode with the 5th-4th case. The black line was obtained from the LST under the same conditions. The resolution was verified, in Fig. 3(left), by comparing the variations of the growth rate for the axial velocity disturbance among the four

Table 1: Grid points

| | $N_x \times N_y \times N_z$ |
|---|---|
| Case A | $601 \times 87 \times 87$ |
| Case B | $601 \times 121 \times 121$ |
| Case C | $601 \times 171 \times 171$ |
| Case D | $601 \times 251 \times 251$ |

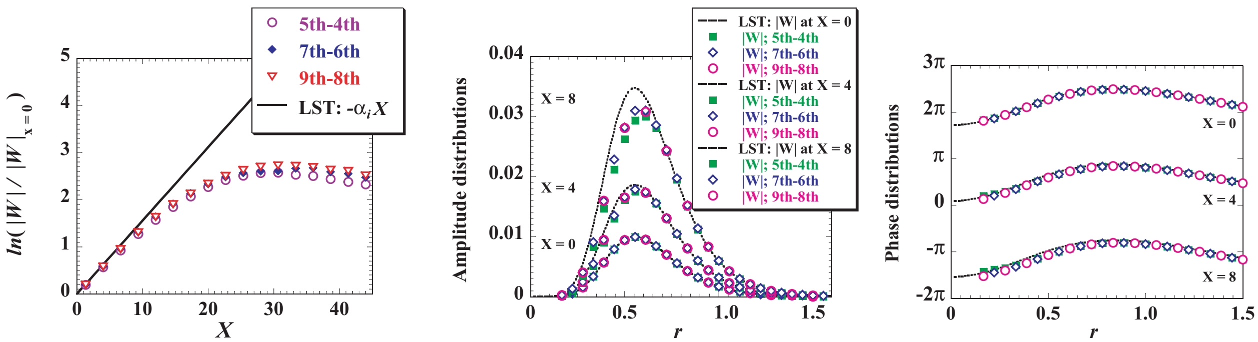


(a) (b)

Figure 4: Comparison of the results from the LST and numerical simulation for the growth rate and the eigenfunction profile (axial velocity disturbance) of the unstable mode $m = -6$ at $M_\infty = 2.5$, $q = 0.16$, and $\mu = 0.5$. (a) Growth rate, $-\alpha_i$; (b) amplitude and phase distributions of the disturbance.

grids listed in Table 1. In terms of evolution of the normal mode, there was little difference between case C and case D during the growth stage without the appearance of small scales resulting from nonlinearity development. Figure 3(right) plots, for case C, $-\alpha_i x = \ln(|\phi|/|\phi|_{x=0})$, where $\phi = R, U, V, W, P$, and $\Omega_x$ are disturbances in density, radial velocity, azimuthal velocity, axial velocity, and axial vorticity, respectively. In the initial stage, the growth rate was in agreement with the spatial growth rate of the inviscid LST because of the large Reynolds number. The result indicates that the vortex had a linear growth to the normal mode during the initial stage of development. (Although not shown in this paper, in case A, the linear growth property was not able to achieve even the 9th-8th accuracy.)

Figure 4(a) plots, for case C, the growth rate obtained by integrating the amplitude profile of the axial velocity disturbance and, in Fig. 4(b), the eigenfunction (amplitude and phase) profiles of the disturbances obtained from the numerical simulation are compared with those obtained from the LST. Each result shows that the linear growth region was around $x \approx 4$, regardless of the different accuracies. Although the disturbance amplitudes for 7th-6th and 9th-8th coincide at $x = 8$, the difference between them appears at $x \approx 20$. Thus, in an early stage, the development of $m = -6$ mode depends on the grid resolution rather than the numerical accuracy.

Figure 5(left) shows the developed vortex structures for 5th-4th, 7th-6th, and 9th-8th using the isosurfaces of the second invariant of the velocity gradient tensor. As mentioned above, the linear stage can be sufficiently captured by using 5th-4th. The initial development part of the spiral structures is clearly similar in each accuracy; however, each case differs in the spatial evolution beyond the middle region. In particular, for the 9th-8th case, small scales around the spiral structures are developed from the high wavenumber mode $m = -6$ and occur downstream, contributing to the different outcome. For $x > 20$, the contour lines of axial vorticity ($y$–$z$ cross section) in streamwise vortices in three $x$-planes perpendicular to the mainstream are shown in Fig. 4(right). The development of the axial vorticity in the plane is similar to that of the incompressible Batchelor vortex in the evolution of normal modes [15]. This suggests that the compressibility effect is small in a plane perpendicular to the main flow and shows the advantage of streamwise vortices. In the three accuracies cases, all the developing vortical structures are similar in $x < 20$ while they show different structures at $x > 40$. In 7th-6th and 9th-8th cases, small eddies occur near the central axis at $x = 40$, and many positive and negative vorticities are observed at $x = 120$.

To observe the internal structures in detail, Fig. 6 presents the helicity density contours, $h = u_i\,\omega_i$ (where $\omega_i$ are the vorticity components), in the $x$–$z$ cross sections through the vortex axis, the positive and negative helicities are rendered in black and white, respectively. Helicity contours are very effective in understanding the transition processes of streamwise vortices [27]. In the early stage, spiral structures generated around the vortex are expressed as negative helicities (white). In the intermediate stage, negative helicities also appear near the axis. For the 5th-4th case, the structures remain at the outer region away from the axis, even downstream. On the other hand, for the 9th-8th case, the structures are disrupted downstream. When such small-scales appear near the vortex axis, they influence each other inside and outside the vortex, and

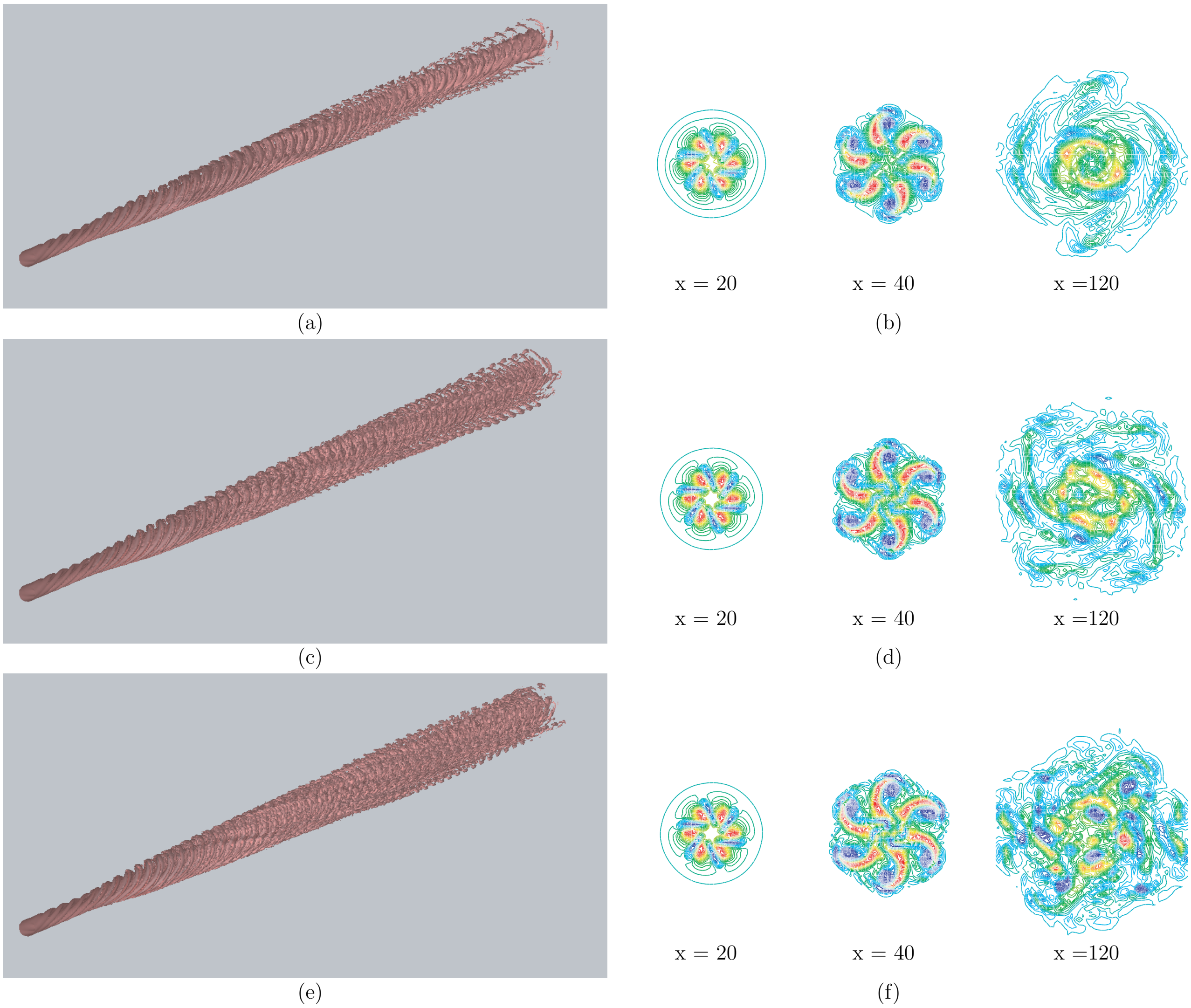


Figure 5: (Left) Isosurfaces of the second invariant of the velocity gradient tensor and (right) contour lines of the axial vorticities $\omega_x$ in three planes perpendicular to the axial flow in case C, (a) and (b) represent the 5th-4th case, (c) and (d) the 7th-6th case, and (e) and (f) the 9th-8th case.

irregular eddies increase downstream. The results suggest that the 9th-8th case has a certain resolution in small vortical structures and could result in a meaningful physical quantity downstream.

According to Figs. 5 and 6, the vortices change the structural look. The streamwise variations in the total circulations $\Gamma$ are shown in Fig. 7(a). The angular momenta in vortices are conserved regardless of the accuracy because of the high Reynolds numbers. Negative vorticities always appear in disturbance development and are also important for going through a turbulent transition. The ratio of positive-to-negative circulations is defined by

$$\frac{\Gamma^-}{\Gamma^+} = \frac{\displaystyle\int_{A^-} \omega_x \, dA^-}{\displaystyle\int_{A^+} \omega_x \, dA^+}, \quad A = \left\{ \begin{array}{ll} A^+, & (\omega_x > 0) \\ A^-, & (\omega_x < 0) \end{array} \right. , \tag{23}$$

where $A$ is the cross-sectional area in a plane perpendicular to the axial flow. Figure 7(b) plots the ratio of positive-to-negative circulations $\Gamma^-/\Gamma^+$ as a function of streamwise distance using Eq. (23) for various

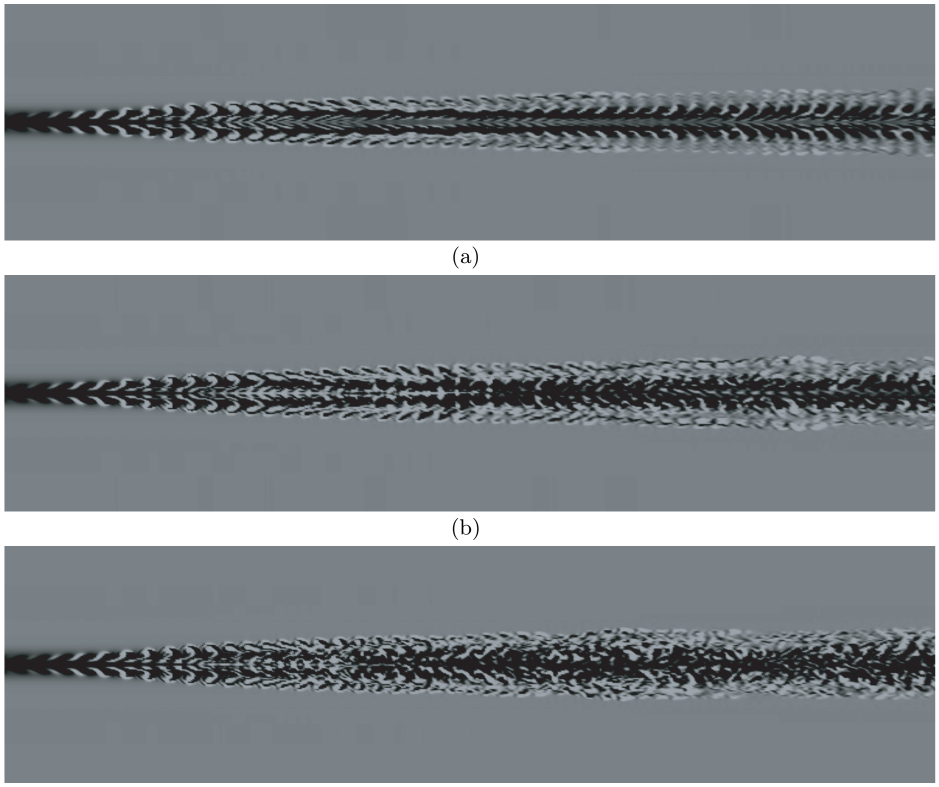

(a)

(b)

(c)

Figure 6: Transition processes of streamwise vortices described by the helicity density contours in the cross sections through the vortex axis in case C, for (a) 5th-4th, (b) 7th-6th, and (c) 9th-8th order accuracy. Positive and negative helicities are rendered in black and white, respectively.

accuracies. The generation of negative circulation is related to a centrifugal instability [7, 15]. Each production of negative circulation coincides at $x < 20$, but otherwise they differ. The amount of the produced $\mathit{\Gamma}^-$ increases with increasing the numerical accuracy. The properties shown in these $\mathit{\Gamma}^-/\mathit{\Gamma}^+$ plots do not contradict the images of the vortical structures in Figs. 5 and 6 (e.g., the negative axial vorticities and helicities). For the 9th-8th case, note that the difference between case C and case D is small.

To compare the effect of small vortical structures generated downstream, the fluctuation growth was evaluated using the total fluctuation energy $\hat{E}$ given as follows [18, 28]:

$$\hat{E} = \hat{K} + \hat{P} + \hat{S}, \tag{24}$$

$$\hat{K} = \frac{1}{2}\overline{\rho}\,\hat{u}_{kk}^2, \quad \hat{P} = \frac{1}{2}\frac{\hat{p}^2}{\gamma\,\overline{p}}, \quad \hat{S} = \frac{1}{2}\frac{\overline{p}}{\gamma(\gamma-1)}\hat{s}^2, \quad \hat{s} = \frac{\hat{p}}{\overline{p}} - \gamma\frac{\hat{\rho}}{\overline{\rho}},$$

The ($\overline{\phantom{x}}$) and ($\wedge$) symbols denote the mean and fluctuating components, respectively, $\hat{K}$ is the fluctuation kinetic energy, $\hat{P}$ is the fluctuation pressure energy, $\hat{S}$ is the fluctuation entropy energy, and $\hat{s}$ is the entropy fluctuation. The total $\hat{E}$ integrated over the cross-sectional area perpendicular to the axial flow is plotted in Fig. 8. The spatial developments of $\hat{E}$ for 5th-4th, 7th-6th, and 9th-8th in case C are shown in Fig. 8(a). Each case differs in character as Fig. 7(b). The energy profile of 5th-4th is lower than the others and is suggested to be incapable of extracting energy from within the vortex core for fluctuation maintenance. For the 9th-8th case, the effect of the grid resolution is shown in Fig. 8(b). In terms of total fluctuation energy, there is not a large difference between case C and case D during the nonlinearity development. Hence, case C grid should be reasonable for producing downstream structures by adding the 9th-8th scheme.

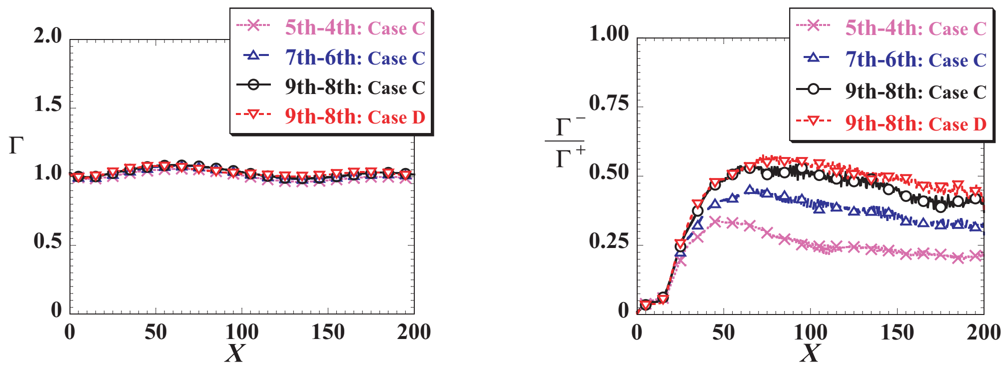


(a) (b)

Figure 7: Spatial developments of (a) total circulation $\Gamma$ and (b) circulation ratios $\Gamma^{-}/\Gamma^{+}$ for various accuracies.

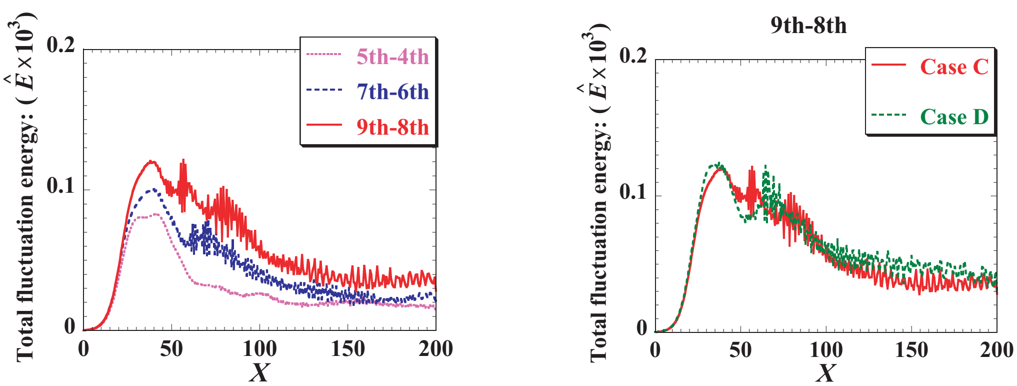


(a) (b)

Figure 8: Total fluctuation energies for (a) case C grid and (b) 9th-8th in case C and D grids.

# 6 Conclusions

Spatial developments of supersonic Batchelor vortices with a linear unstable mode for $m = -6$ as a high-wavenumber, were numerically simulated at Mach number 2.5 using a WCNS scheme for three different accuracies. During the early stage, the growth rate and eigenfunction profiles of the disturbance obtained by numerical calculations were generally consistent with those obtained from the LST, regardless of the computational accuracy. In the nonlinear developments, however, the results differed from accuracy to accuracy. Under the same grid resolution, the ninth-order accuracy scheme for the interpolation of primitive variables has much better property in capturing small-scales compared to the others. When using the high-order scheme, the streamwise vortex came to chaotic dynamics at the downstream in the $m = -6$ mode evolution. Note that the isentropic vortices lead to the generation of small-scales in a supersonic flow, where disturbance growth is strongly suppressed by compressibility effects. In this respect, the numerical simulation with a high accuracy appears promising to resolve the developed flow. As a future work, the effects of viscosity on disturbance development in supersonic flows, which is an important problem, and the relation between the Mach number and the Reynolds number, should be investigated.

# Acknowledgments

This work was partly achieved through the use of large-scale computer systems SX-ACE at the Cybermedia Center, Osaka University and was supported by JSPS KAKENHI grant number JP17K05145.

## References


[1] E. T. Curran, W. H. Heiser, and D. T. Pratt. Fluid phenomena in scramjet combustion systems. *Ann. Rev. Fluid Mech.*, 28(1):323–360, 1996.

[2] P. E. Dimotakis. Turbulent free shear layer mixing and combustion. In S. Murthy and E. Curran, editors, *High Speed Flight Propulsion Systems*, volume 137, pages 265–340. AIAA, 1991.

[3] D. Bogdanoff. Compressibility effects in turbulent shear layers. *AIAA J.*, 21:926–927, 1983.

[4] D. Papamoschou and A. Roshko. The compressible turbulent shear layer experimental study. *J. Fluid Mech.*, 197:453–477, 1988.

[5] N. T. Clemens and M. G. Mungal. Large-scale structure and entrainment in the supersonic mixing layer. *J. Fluid Mech.*, 284:171–216, 1995.

[6] C. Pantano and S. Sarkar. A study of compressibility effects in the high-speed turbulent shear layer using direct simulation. *J. Fluid Mech.*, 451:329–371, 2002.

[7] T. Hiejima. Spatial evolution of supersonic streamwise vortices. *Phys. Fluids*, 26:074102, 2014.

[8] G.-S. Jiang and C.-W. Shu. Efficient implementation of weighted ENO schemes. *J. Comput. Phys.*, 126(1):202–228, 1996.

[9] Q. Li, Y. Yan, Ping Lu, A. Pierce, C. Liu, and F. Lu. Numerical and experimental studies on the separation topology of the MVG controlled flow at M = 2.5. *AIAA Paper No. 2011–72*, 2011.

[10] X. Deng and H. Zhang. Developing high-order weighted compact nonlinear schemes. *J. Comput. Phys.*, 165(1):22–44, 2000.

[11] S. Zhang, S. Jiang, and C.-W. Shu. Development of nonlinear weighted compact schemes with increasingly higher order accuracy. *J. Comput. Phys.*, 227(15):7294–7321, 2008.

[12] T. Nonomura and K. Fujii. Robust explicit formulation of weighted compact nonlinear scheme. *Comp. Fluids*, 85(Supplement C):8–18, 2013.

[13] Z.-G. Yan, H. Liu, Y. Ma, M. Mao, and X. Deng. Further improvement of weighted compact nonlinear scheme using compact nonlinear interpolation. *Comp. Fluids*, 156:135–145, 2017. Ninth International Conference on Computational Fluid Dynamics (ICCFD9).

[14] T. Hiejima. Criterion for vortex breakdown on shock wave and streamwise vortex interactions. *Phys. Rev. E*, 89:053017, 2014.

[15] I. Delbende and M. Rossi. Nonlinear evolution of a swirling jet instability. *Phys. Fluids*, 17:044103, 2005.

[16] M. Abid. Nonlinear mode selection in a model of trailing line vortices. *J. Fluid Mech.*, 605:19–45, 2008.

[17] M. S. Broadhurst and S. J. Sherwin. Helical instability and breakdown of a Batchelor trailing vortex. In *Prog. in Industrial Mathematics at ECMI 2006. Mathematics in Industry*, pages 191–195. Springer, 2008.

[18] T. Hiejima. Streamwise vortex breakdown in supersonic flows. *Phys. Fluids*, 29:054102, 2017.

[19] G. K. Batchelor. Axial flow in trailing line vortices. *J. Fluid Mech.*, 20:645–658, 1964.

[20] J. W. Naughton, L. N. Cattafesta, and G. S. Settles. An experimental study of compressible turbulent mixing enhancement in swirling jets. *J. Fluid Mech.*, 330:271–305, 1997.

[21] T. Hiejima. Linear stability analysis on supersonic streamwise vortices. *Phys. Fluids*, 25:114103, 2013.

[22] Y. Wada and M.-S. Liou. A flux splitting scheme with high-resolution and robustness for discontinues. *AIAA Paper No. 94–0083*, 1994.

[23] R. Borges, M. Carmona, B. Costa, and W. S. Don. An improved weighted essentially non-oscillatory scheme for hyperbolic conservation laws. *J. Comput. Phys.*, 227(6):3191–3211, 2008.

[24] M. Castro, B. Costa, and W. S. Don. High order weighted essentially non-oscillatory WENO-Z schemes for hyperbolic conservation laws. *J. Comput. Phys.*, 230(5):1766–1792, 2011.

[25] A. Jameson, W. Schmidt, and E. Turkel. Numerical simulation of the Euler equations by finite volume method using Runge–Kutta time stepping schemes. *AIAA paper No. 81–1259*, 1981.

[26] T. Hiejima. Theoretical analysis of streamwise vortex circulation induced by a strut injector. *Phys. Rev. Fluids*, 1:054501, Sep 2016.

[27] T. Hiejima. A factor involved in efficient breakdown of supersonic streamwise vortices. *Phys. Fluids*, 27:034103, 2015.

[28] A. Hanifi, P. J. Schmid, and D. S. Henningson. Transient growth in compressible boundary layer flow. *Phys. Fluids*, 8(3):826–837, 1996.